# Insights into the charge carrier dynamics in perovskite/Si tandem solar cells using transient photocurrent spectroscopy

Anaranya Ghorai,[1] Prashant Kumar,[1] Suhas Mahesh,[2] Yen-Hung Lin,[2] Henry J. Snaith,[2] and K. S. Narayan[1,a]

**AFFILIATIONS**

[1]Chemistry and Physics of Materials Unit and School of Advanced Materials,
Jawaharlal Nehru Center for Advanced Scientific Research, Jakkur, Bengaluru 560064, India
[2]Clarendon Laboratory, Department of Physics, University of Oxford, Oxford OX1 3PU, United Kingdom

[a]Author to whom correspondence should be addressed: narayan@jncasr.ac.in

**ABSTRACT**

Direct bandgap perovskite and indirect bandgap Si, which form the two active layers in a tandem solar cell configuration, have different optoelectronic properties and thicknesses. The charge-carrier dynamics of the two-terminal perovskite-on-Si tandem solar cell in response to a supercontinuum light pulse is studied using transient photocurrent (TPC) measurements. Spectral dependence of TPC lifetime is observed and can be classified into two distinct timescales based on their respective carrier generation regions. The faster timescale ($\sim$500 ns) corresponding to the spectral window (300–750 nm) represents the top-perovskite sub-cell, while the slower timescale regime of $\sim$25 $\mu$s corresponds to the bottom-Si sub-cell ($>$700 nm). Additionally, under light-bias conditions, the transient carrier dynamics of the perovskite sub-cell is observed to be coupled with that of the Si sub-cell. A sharp crossover from the fast-response to a slow-response of the device as a function of the light-bias intensity is observed. These results along with a model based on transfer matrix formulation highlight the role of charge-carrier dynamics in accessing higher efficiencies in tandem solar cells. The carrier transit times and lifetimes in addition to their optical properties need to be taken into account for optimizing the performance.

*Published under an exclusive license by AIP Publishing.* https://doi.org/10.1063/5.0080109

Power conversion efficiencies (PCEs) of hybrid organic–inorganic perovskite (HOIP) single-junction solar cells have gone as high as 25.7%.[1] Owing to the easy bandgap tunability of perovskite coupled with such high efficiencies make them the most promising candidate to be used for tandem solar cells, which consist of two solar cells (one wide bandgap and one narrow bandgap) connected in series using a recombination layer. The power conversion efficiencies (PCEs) for all-perovskite tandem cells have reached 26.4%,[2] 24.2% for perovskite/CIGSe (copper–indium–gallium-selenide) tandem cells,[1,3,4] and 29.5% for perovskite-on-silicon tandem cells.[5] The easy processability of perovskite solar cells provides facile deposition on silicon solar cells and can increase the efficiencies of commercial photovoltaics (PVs), maintaining the economics of scaling.[6] The efficiency limits of these perovskite-based tandem solar cells are well above 30% and provide much scope for further improvement.[7]

The efficiency of a tandem solar cell strongly depends on the absorbency of the active layers in each of the sub-cells, the interfacial and bulk traps or defects present in the active materials which can reduce the charge-carrier collection, and the inter sub-cell current matching condition.[8] The tandem solar cells are then generally designed and fabricated based on the optical characteristics of each of the active materials in respective sub-cells. The bandgap of the top perovskite sub-cell is tailored in such a way (theoretically in the range of 1.6–1.75 eV)[9–12] that the optimum efficiency is reached when coupled to a silicon sub-cell. It was observed that a perovskite bandgap of 1.66 eV with an active layer thickness of 500 nm was optimum for arriving at the current matching condition.[13,14] We explore the possibility of further fine-tuning the sub-cells by controlling their carrier dynamics. The coupling of the two sub-cells in series makes it difficult to deconvolve the dynamics in the sub-cells necessary for optimization of the tandem solar cells.

This paper provides insight into the charge-carrier dynamics in the individual sub-cells using transient photocurrent (TPC) spectroscopy in the tandem configuration, which helps us to understand the generation and recombination dynamics of charge-carriers in complete tandem devices. The TPC measurements help us in assessing the
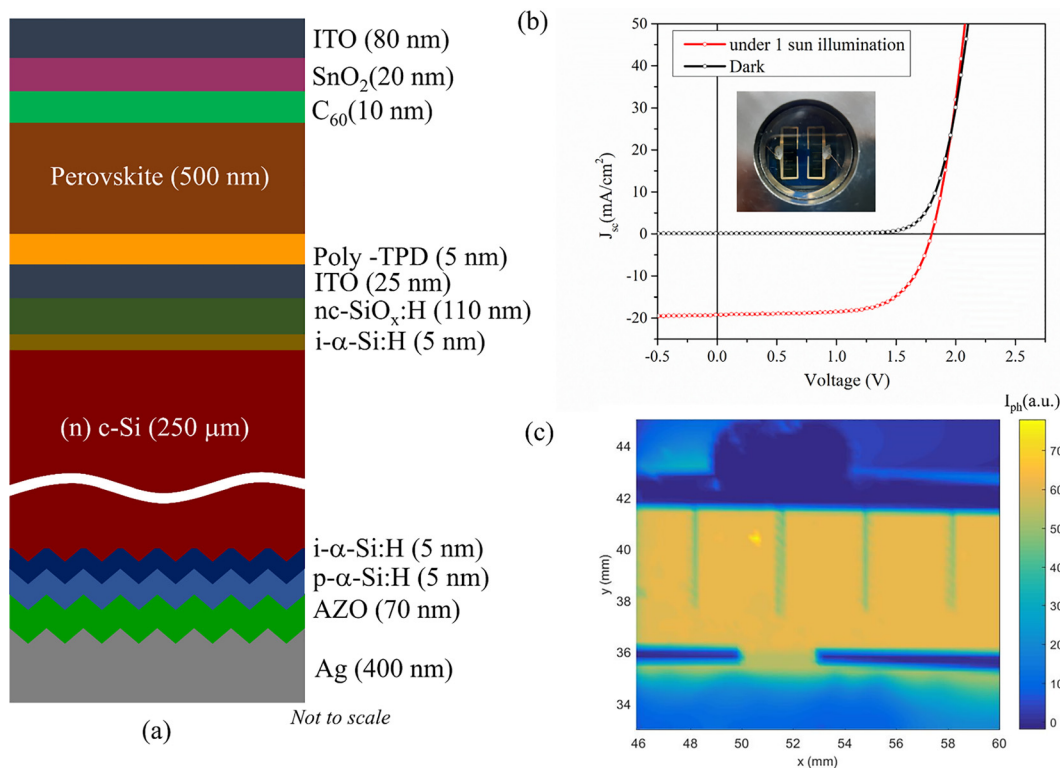
**FIG. 1.** (a) Device architecture of the two-terminal perovskite/Si tandem solar cell, (b) typical J–V characteristics of the tandem solar cell under simulated AM 1.5G (100 mW/cm$^2$) illumination (the inset shows the picture of the tandem device), and (c) a 2D LBIC image.

timescales of photogenerated charge carriers getting extracted from the electrodes. The pathway for losses in external quantum efficiency (EQE) via recombination (both radiative and non-radiative) can be directly probed by TPC. When a short pulse (<1 ns) is used as the excitation source, the generation duration can be considered almost instantaneous, as compared to the other processes in the device (namely, recombination and carrier dynamics). The current due to photogenerated excess carriers ($\delta n$) can be expressed as[15]

$$I = \frac{d(\delta n)}{dt} = D\frac{\partial^2(\delta n)}{\partial x^2} + \mu E \frac{\partial(\delta n)}{\partial x} - R, \quad (1)$$

where $R$ is the recombination term and $D$ and $\mu$ are the diffusion coefficient and mobility of carriers, respectively. In the case of thick silicon cells, $E \approx 0$, which attributes to the diffusion limited transport in Si. However, in the case of perovskites, there are contributions from both carrier recombination lifetime as well as the carrier-transit time in the TPC profiles. The response profiles of the TPC as a function of different parameters under a model framework can explain the performance of tandem solar cells under continuous white-light excitation.

The details of the fabrication protocol[16] for the tandem solar cell are given in the supplementary material (Sec. 11). The final device structure of the fabricated tandem solar was ITO (80 nm)/SnO$_2$ (20 nm)/C$_{60}$(10 nm)/Cs$_{0.05}$(FA$_{0.83}$MA$_{0.17}$)$_{0.95}$Pb(I$_{0.77}$Br$_{0.23}$)$_3$(500 nm)/Poly-TPD (5 nm)/ITO (25 nm)/nc-SiO$_x$:H (110 nm)/i-$\alpha$-Si:H (5 nm)/n-c-Si (250,000 nm)/i-$\alpha$-Si:H (5 nm)/p-$\alpha$-Si:H (5 nm)/AZO (70 nm)/

Ag (400 nm). Figure 1(a) shows the device architecture of the tandem solar cell with an active area of 1.1 cm$^2$. The J–V characteristics [Fig. 1(b)] of the tandem solar cell under simulated AM1.5G (100 mW/cm$^2$) illumination were performed for the determination of typical solar cell parameters. These parameters are listed in Table I.

Light-beam induced current (LBIC) imaging of the solar cell verifies the active area and the degree of homogeneity.[17] LBIC images directly highlight the presence of defective regions.[18–20] The images was obtained from a 650 nm source with a 270 $\mu$m resolution (Fig. S8) shown in Fig. 1(c) reveals the homogenous spatial contribution from both sub-cells to the short circuit current. It also shows a uniform charge-carrier generation region throughout the device. PL imaging (Fig. S9) of the device also validated the uniformity of carrier generation in the device.

The TPC measurements are conventionally done under short-circuit conditions (50 $\Omega$ coupling).[21–24] A series of TPC measurements were carried out at different $\lambda$. Figure 2 represents a set of results corresponding to the perovskite sub-cell (500, 625, and 750 nm) and Si sub-cell (750, 850, 975, and 1100 nm) spectral regions. These

**TABLE I.** Solar cell parameters for the fabricated perovskite:Si tandem solar cell.

| Efficiency | Fill factor | J$_{sc}$ (mA/cm$^2$) | V$_{oc}$ (V) |
|---|---|---|---|
| 23.0% | 66.44% | 19.23 | 1.80 |

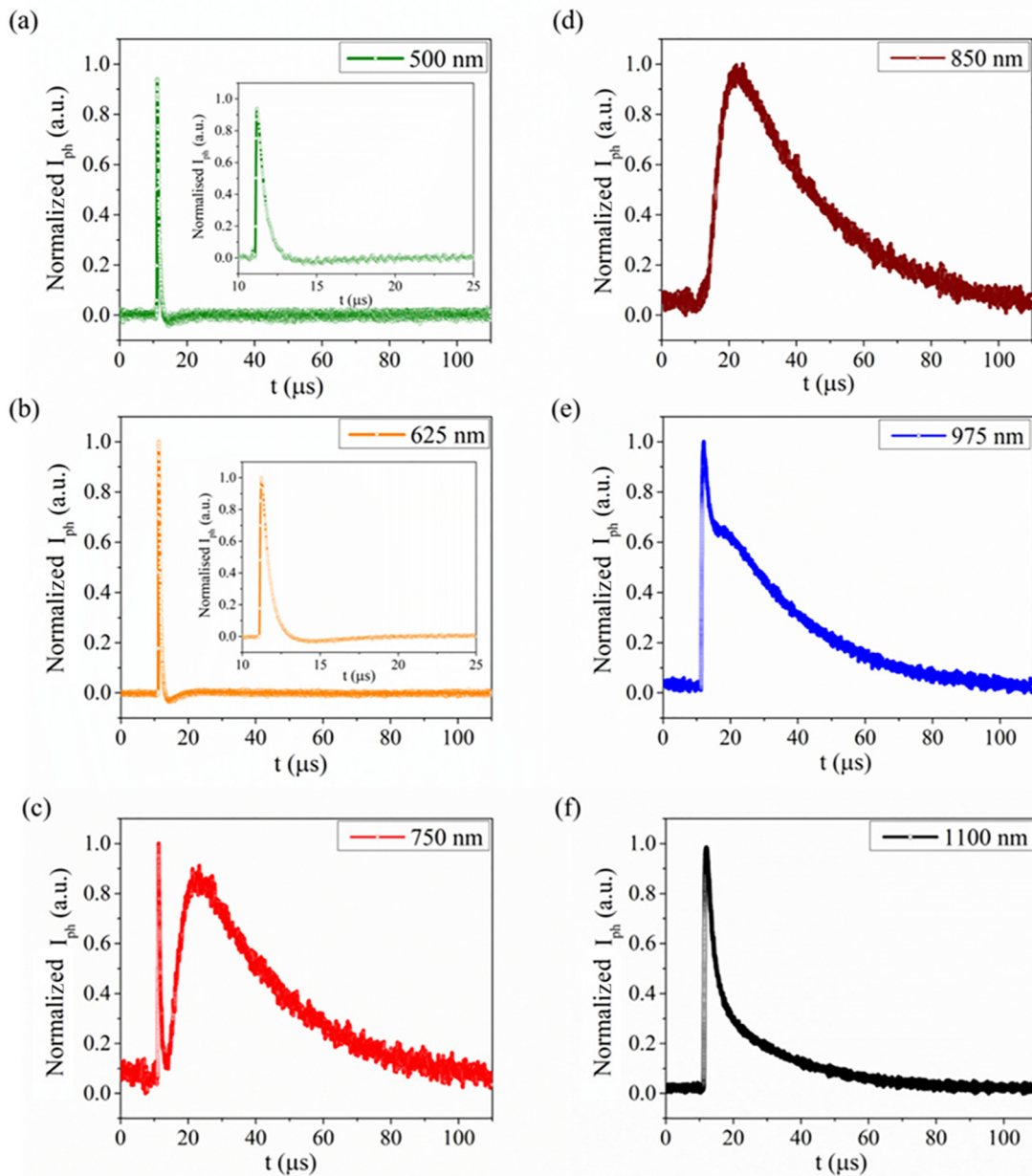**FIG. 2.** Transient photocurrent profiles of the tandem solar cell for excitation $\lambda$s of (a) ~6.21 $\mu$W 500 nm and (b) ~11.78 $\mu$W 625 nm, insets show the magnified TPC profile (c) ~6.53 $\mu$W 750 nm, (d) ~9.4 $\mu$W 850 nm, (e) ~10.9 $\mu$W 975 nm, and (f) ~66.54 $\mu$W 1100 nm (measured in the short circuit-condition at 50 $\Omega$ coupling using a supercontinuum picosecond pulse coupled with an acousto-optic tunable filter providing 20 nm spectral windows).

measurements were also carried out with different background light intensities and electrical bias conditions.

The differences in the carrier dynamics of the sub-cells are clearly evident in the $\lambda$ dependence of $I_{ph}(t)$ as shown in Fig. 2. The dynamics of the photogenerated carriers in the perovskite sub-cell [Figs. 2(a) and 2(b)] dominates the TPC response in the high-energy spectral region (<700 nm). Even though the $I_{ph}(t)$ for the perovskite sub-cell in the tandem cell consists of multiple contributions, the decay is dominantly described by a single exponential. The corresponding TPC lifetime $\tau_1$ is obtained by fitting the decay profiles to single exponentials in this spectral region with $\tau_1 \approx 500$ ns [Figs. 2(a) and 2(b)]. The dynamics of the photogenerated carriers in the silicon sub-cell [Figs. 2(d) and 2(e)] dominates the TPC in the lower energy spectral region (>750 nm) with a slower decay lifetime of $\approx 25$ $\mu$s. The intermediate region (750 nm excitation) as shown in Fig. 2(c) shows the distinct contributions of TPC profiles that arise from both the perovskite as

well as Si sub-cells. The transient photocurrent decay in both spectral regions can be modeled as a single exponential reasonably, and a distinct crossover from the carrier relaxation processes in the perovskite layer to Si sub-cells as a function of incident light $\lambda$ can be observed. The TPC profile corresponding to the perovskite sub-cell reduced considerably beyond 700 nm and is negligible beyond 800 nm of excitation. Thus, for $\lambda > 800$ nm, the TPC profiles represent the Si sub-cell response exclusively. In the region $\lambda > 900$ nm, the TPC decay profile evolved from being a single exponential to a bi-exponential decay given by $I_{ph}(t) = B \exp(-t/\tau_2) + C \exp(-t/\tau_3) + d$ with $\tau_2$ continuing to be in the range of $\sim 25\ \mu s$ and $\tau_3 \sim 2\ \mu s$ [Fig. 2(f)]. The variation of TPC lifetimes corresponding to Si ($\tau_2$ and $\tau_3$) with $\lambda$ is shown in Fig. 3(c).

The three timescales $\tau_1$, $\tau_2$, and $\tau_3$, can be interpreted in terms of the multilayered structure using a transfer-matrix optical model.[25] The scattering matrices for each layer in the tandem solar cell were derived for each wavelength from their corresponding refractive index dispersion curves using MATLAB. The scattering matrices for each layer were combined using Redheffer star product to derive a device scattering matrix for each wavelength. They were then connected to the transmission and reflection regions to generate a global scattering matrix. Figure 3(a) shows the fraction of light absorbed by the

individual sub-cell of perovskites and Si. The fraction of light reflected from the whole tandem cell is also indicated in Fig. 3(a). The internal field matrix consisting of the magnitudes of both the electric and magnetic fields is given by $\psi(z') = W \exp(\lambda z')c$, where W is the square eigenvector matrix whose column vectors describe the modes that can exist in each layer, $\exp(\lambda z')$ is a diagonal matrix that describes the accumulation of the phase as the waves propagate, and c quantifies the amount of power in each mode. Thus, the internal electric fields were calculated for each of the layers from the scattering matrices generated for each layer. These internal electric field profiles were generated for the $\lambda$ ranging from 500 nm and 1100 nm. The charge-carrier generation at each of the layers is proportional to the square of the modulus of the internal electric field and expressed as[26,27]

$$G = \frac{\lambda}{hc}Q \quad \text{with} \quad Q = \frac{4\pi c \epsilon_0 k(\lambda)n(\lambda)}{2\lambda}|E(x)|^2, \qquad (2)$$

where $k(\lambda)$ and $n(\lambda)$ are the real and imaginary parts of the refractive index, respectively. The variation of n and k for the active layers of perovskites and Si as a function of $\lambda$ is given in Fig. S5.

The carrier generation profiles for both the perovskite layer and the Si layer are estimated for different $\lambda$ (Figs. S6 and S7). The charge-carrier generation profile inside the Si active layer for 925 nm is shown
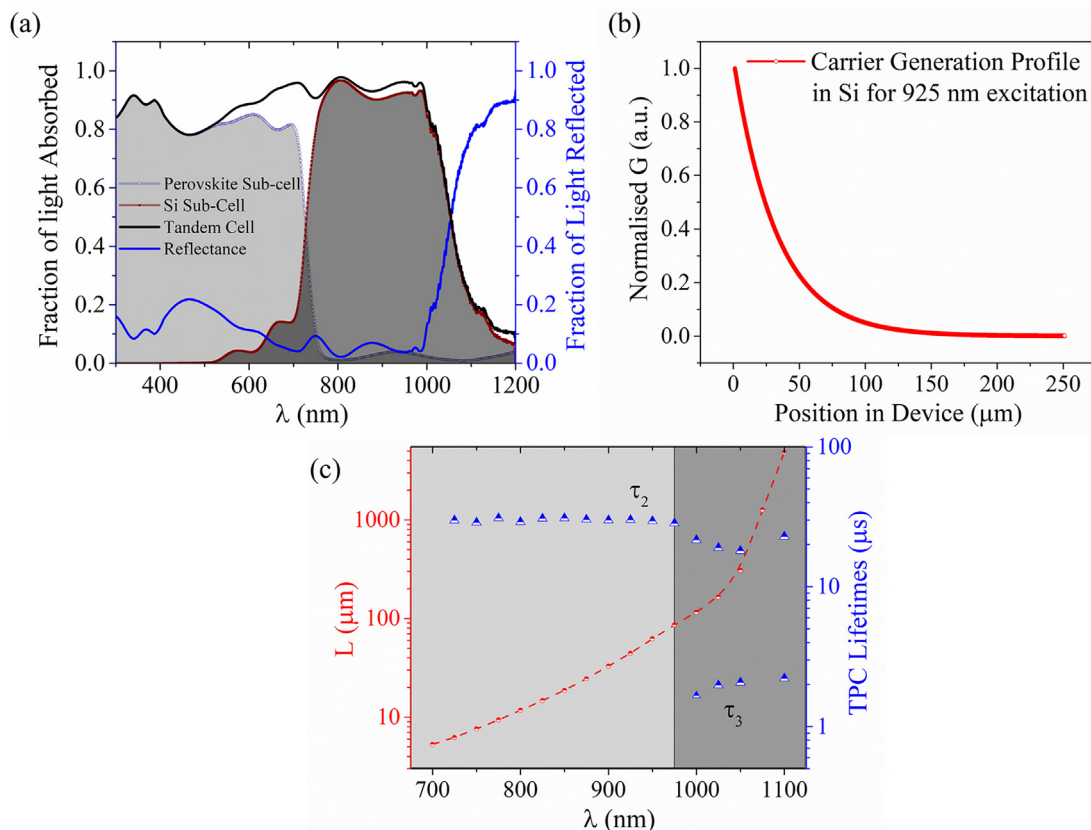


**FIG. 3.** (a) Fraction of light absorbed by the perovskite sub-cell, the Si sub-cell, and the tandem cell plotted in the left y-axis; fraction of light reflected from the tandem cell plotted in the right y-axis (both derived from the transfer matrix formalism). (b) Charge-carrier generation profile in Si for excitation at 925 nm derived from the transfer matrix formalism. (c) L as a function of $\lambda$ inside the Si sub-cell derived from the transfer matrix formalism (left y-axis); variation of TPC lifetimes ($\tau_2$ and $\tau_3$) with $\lambda$ (right y-axis).

in Fig. 3(b). From the carrier generation profiles for Si, a parameter of excess carrier density decay length, L is determined by fitting a single exponential. A lower L magnitude is indicative of the larger distance of the charge-carrier generation region from the electrode. Figure 3(c) shows the nonlinear variation of L with $\lambda$ with a drastic rise beyond 1000 nm. Thus, for $\lambda > 950$ nm, more charge-carriers are generated near the electrode in contrast to lower wavelengths, thus creating an initial charging at the electrode. This gives rise to a quite observable displacement current with lifetime $\tau_3$ for the $\lambda > 950$ nm. The inverse effect considering the perovskite sub-cell can also be observed where a negative displacement current is observed for the wavelength range $\lambda < 650$ nm as more charges are generated near the top electrode.

In the case of the $I_{ph}(t)$ response to incident monochromatic light exciting the perovskite sub-cell, the finite shunt value of the Si sub-cell in the dark provides the pathway to the current. The ratio of the shunt resistances $(R_{sh1}/R_{sh2})$ is $\sim$1:13 as obtained from $\lambda$ dependent TPC measurements. Thus, the shunt resistance corresponding to the Si sub-cell is an order of magnitude higher than the perovskite sub-cell as

also seen in the literature.[28] The introduction of light-bias during $I_{ph}(t)$ measurement opens up transport in both cells and increases the magnitude of $I_{ph}(t)$. The TPC lifetime $\tau_1$ shows an abrupt transition from $\sim$500 ns to 4.5 $\mu$s as the background light bias excitation of the Si sub-cell is increased [Fig. 4(b)]. This observation can be described using an equivalent circuit model.[8,29] The current generated in a sub-cell is given as $I_i = I_{Di} + I_{shi} - I_{phi}$. $I_{phi}$ consists of the photocurrent generated by external illumination in the $i$th sub-cell. $I_{Di}$ is the current across the diode, $D_i$ and is given by $I_{Di} = I_{Di}^0 \left[ \exp\left( -\frac{eV_i}{mk_BT} \right) - 1 \right]$ with $m > 1$. Here, $V_i$ is the voltage across the $i$th sub-cell with $k_BT/e$ being the thermal voltage. $I_{shi}$ is the current flowing through the shunt resistance of the $i$th sub-cell.

In the absence of background light bias, $\tau_1$ is primarily decided by the carrier dynamics in the charge-generating regions, which is the perovskite in this case. The magnitude of the TPC is, however, dominantly governed by the shunt resistance of the other sub-cell $(R_{sh2})$. This is because $D_2$ is in the reverse bias condition and $I_{D2}$ is composed
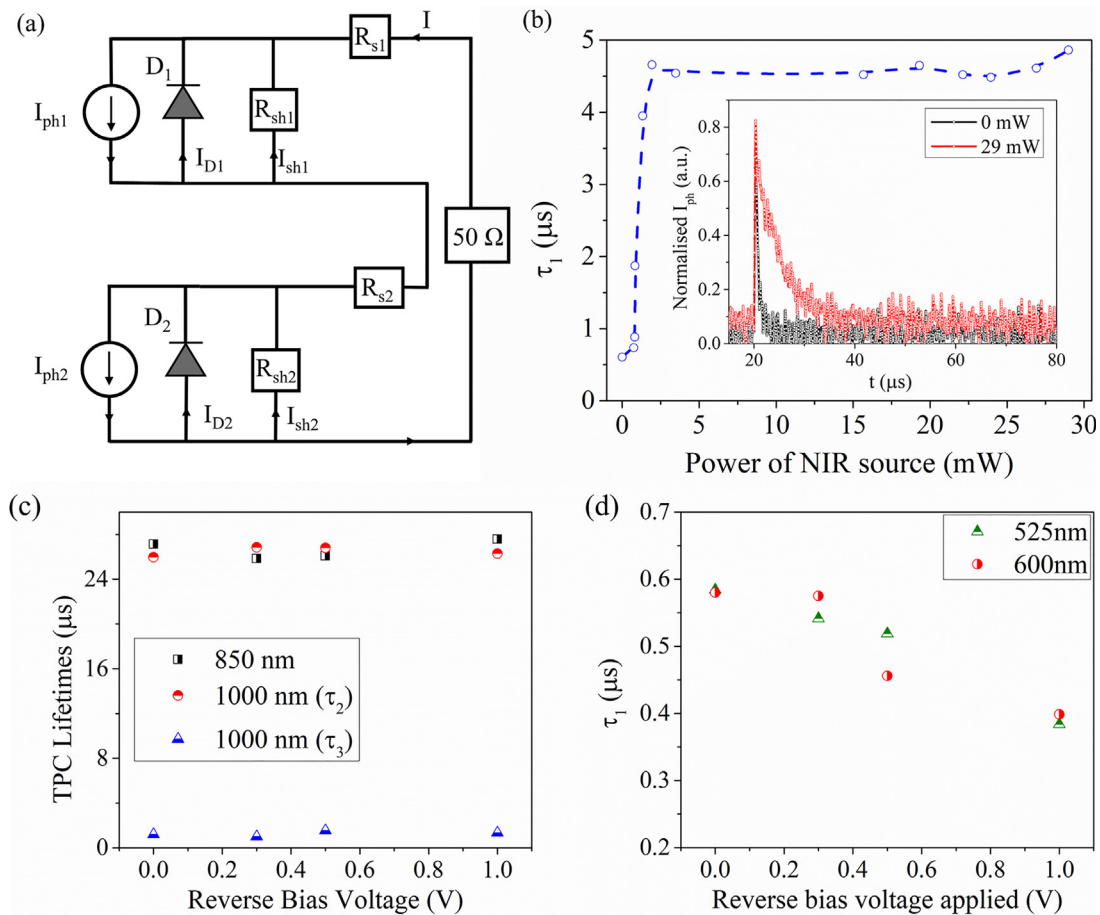


**FIG. 4.** (a) Equivalent circuit for a tandem solar cell with series-connected sub-cells. The positive direction of current flow is indicated by an arrow in each branch, and $R_{Shi}$ represents the shunt resistance in cell i. (b) Variation of $\tau_1$ corresponding to $\sim$6.32 $\mu$W 550 nm pulsed excitation with the intensity of background near-infrared (NIR) illumination (700–1100 nm) exciting the Si sub-cell. (The inset shows the comparison of the TPC profile for 29 mW background illumination with no background illumination.) (c) Variation of $\tau_2$ and $\tau_3$ with reverse bias voltage for $\sim$9.41 $\mu$W 850 nm, $\sim$9.51 $\mu$W 1000 nm, and $\sim$66.54 $\mu$W 1100 nm excitations. (d) Variation of $\tau_1$ with reverse bias voltage for $\sim$6.34 $\mu$W 525 nm and $\sim$8.32 $\mu$W 600 nm.

of current from only the minority carriers in the Si. Thus, the net transient photocurrent, in this case, is $I(t) \approx I_{sh2}(t)$. As the NIR background illumination ($>850$ nm) is increased, $I_{ph2}$ starts increasing, thus forward biasing $D_2$. At sufficiently high background illumination, $V_2$ is large enough to drive $D_2$ as the conducting channel for the photogenerated carriers from the perovskite sub-cell. The total transient photocurrent then is $I(t) \approx I_{D2}(t) + I_{sh2}(t)$ with $I_{D2}$ having contributions from both $I_{ph1}(t)$ and $I_{ph2}(t)$. Thus, the $I(t)$ profile embeds the carrier dynamics of the Si sub-cell in the $I_{D2}(t)$ response along with the already existing $I_{sh2}(t)$. Recombination carrier lifetime in Si is large and is dominantly mediated by the defect centers with $\frac{1}{\tau_{rec}} \approx \frac{1}{\tau_{rad}} + \frac{1}{\tau_{SRH}} + \frac{1}{\tau_{Auger}}$. This creates a much higher time constant for $I(t)$, which is basically the effective time constant derived from $I_{sh2}(t)$ and $I_{D2}(t)$, which explains the abrupt increase in $\tau_1$ by an order of magnitude as the background illumination is increased. In contrast, however, it is observed that $\tau_2$ does not show any change when the Si sub-cell is excited with a picosecond pulse ($\lambda > 800$ nm) while simultaneously light-biasing the perovskite sub-cell with 470 nm excitation (Fig. S3). This is because the time constants associated with the perovskite sub-cell (which is a direct bandgap semiconductor and of much lower thickness) are orders of magnitude lower than the Si sub-cell. These results assert that the carrier dynamics of one sub-cell are decoupled with the other under single sub-cell excitation. However, the carrier dynamics of the sub-cells becomes coupled when both the sub-cells are simultaneously excited and are dominated by the sub-cell having slower charge-carrier dynamics.

The subtle differences in the operation of sub-cells are also evident in studies carried out with an applied reverse bias voltage. For $\lambda > 700$ nm, i.e., the region falling under the Si sub-cell absorption spectrum [Fig. 3(a)], there is no dependence of the TPC lifetime on the applied reverse bias voltage [Fig. 4(c)]. This feature is indicative of the diffusive mode of transport in the Si sub-cell. The excess carrier density from TPC experiments is $\sim10^{15}$, which suggests that the average recombination lifetime of minority carriers forms a component in the decay times along with diffusion limited transport transit time as explained by Eq. (1). However, for the region of $\lambda < 700$ nm, i.e., the region falling under the perovskite absorption spectrum [Fig. 3(a)], there is a clear reduction in the TPC lifetime as the reverse bias voltage is increased [Fig. 4(d)]. This observation is attributed to a considerable drift component in the perovskite sub-cell response enabling a faster extraction. Thus, unlike the Si sub-cell, internal electric fields in the perovskite sub-cell play an important role in the charge-carrier transport. For the perovskite sub-cell, TPC lifetime has contributions from the carrier-transit time (having both drift and diffusion components) as well as from the average carrier-recombination lifetime. The difference in the nature of the charge-carrier transport in the two sub-cells results in the two orders of magnitude difference in the values of $\tau_1$ and $\tau_2$. This contrast in $\tau$ can possibly play a role of limiting the fill-factor of the tandem solar cell.

The TPC measurements directly help us in assessing the time-scales of photogenerated charge carriers getting extracted to the electrodes. Figure 5 summarizes the governing charge carrier extraction dynamics when a targeted sub-cell is excited and when both the sub-cells are operational. The time constants associated with the perovskite sub-cell (which is a direct bandgap semiconductor and of much lower thickness) are orders of magnitude faster than the Si sub-cell. The thickness of the active layers in multijunction solar cells should be optimized in such a way that the recombination losses be
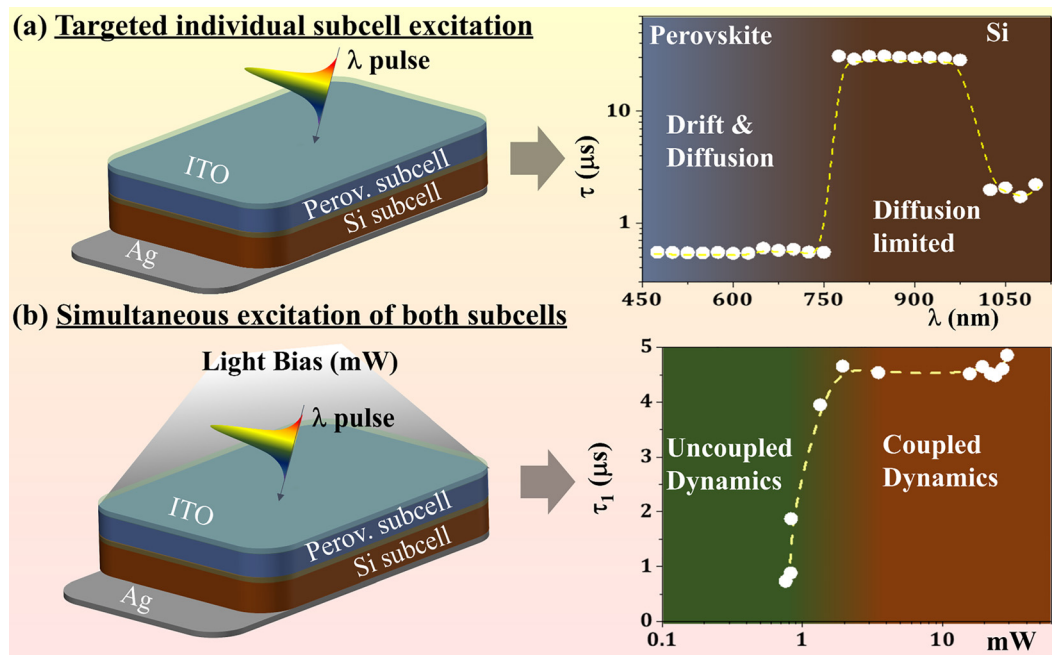


**FIG. 5.** Schematic showing the carrier transport mechanisms in the perovskite/Si tandem solar cell under (a) targeted individual sub-cell excitation (b) when both the sub-cells are simultaneously excited.

minimized, and the highest EQE, fill-factor, and $V_{oc}$ are achieved. Optimization of series resistances, shunt resistances, and surface recombination velocities need to be achieved using TPC spectroscopy for sub-cells for better multi-junction devices with enhanced performance parameters.

In conclusion, we observed a spectral dependence of transient photocurrent lifetime, which can be classified into two distinct timescales. The first timescale, $\tau_1 \sim 500$ ns, represents the absorption in the top perovskite sub-cell ($\lambda -300$–750 nm). The other timescale regime of $\tau_2 \sim 25$ $\mu$s and $\tau_3 \sim 2$ $\mu$s corresponds to absorption in the rear Si sub-cell ($\lambda > 700$ nm). We infer that the transport processes in the perovskite sub-cell are influenced by the high field strength. Hence, the carriers are extracted via both drift and diffusion processes in the perovskite sub-cell, whereas the Si sub-cell follows a diffusion limited carrier extraction process. However, this can lead to ion transport in the perovskite sub-cell, which will have an effect on the degradation process that needs to be examined further. In the absence of background illumination, sub-cell processes are uncorrelated, and the current magnitude is dependent on the shunt resistance of the other sub-cell in the dark. A crossover of the dynamics of the perovskite sub-cell to a coupled-regime with the Si sub-cell beyond a threshold dc-light illumination is observed. Fine-tuning of the two active layer thicknesses can further optimize absorption, carrier transit times, and lifetimes and lead to higher efficiencies.

See the supplementary material for TPC profiles in response to a supercontinuum pulse, $\lambda$ dependent TPC profiles, TPC lifetime for the Si sub-cell under 470 nm background illumination, TPC lifetimes with pulsed excitation intensities, optical constant for Si and perovskites as a function of the wavelength, carrier generation profiles in the perovskite active layer, carrier generation profiles in the Si active layer, beam spot size in LBIC imaging, Si PL image in the tandem structure, EQE of the tandem solar cell, and experimental details (device fabrication protocol, TPC measurement protocol, and LBIC measurement protocol).

## AUTHOR DECLARATIONS
### Conflict of Interest

The authors have no conflicts to disclose.

### DATA AVAILABILITY

The data that support the findings of this study are available from the corresponding author upon reasonable request.

## REFERENCES

[1]See https://www.nrel.gov/pv/cell-efficiency.html for "NREL Best Research-Cell Efficiency Chart."

[2]R. Lin, J. Xu, M. Wei, Y. Wang, Z. Qin, Z. Liu, J. Wu, K. Xiao, B. Chen, and S. M. Park, Nature **603**, 73–78 (2022).

[3]A. Al-Ashouri, A. Magomedov, M. Roß, M. Jošt, M. Talaikis, G. Chistiakova, T. Bertram, J. A. Márquez, E. Köhnen, and E. Kasparavičius, Energy Environ. Sci. **12**, 3356–3369 (2019).

[4]T. Todorov, T. Gershon, O. Gunawan, Y. S. Lee, C. Sturdevant, L. Y. Chang, and S. Guha, Adv. Energy Mater. **5**, 1500799 (2015).

[5]A. Al-Ashouri, E. Köhnen, B. Li, A. Magomedov, H. Hempel, P. Caprioglio, J. A. Márquez, A. B. M. Vilches, E. Kasparavicius, and J. A. Smith, Science **370**, 1300–1309 (2020).

[6]F. Fu, J. Li, T. C. J. Yang, H. Liang, A. Faes, Q. Jeangros, C. Ballif, and Y. Hou, Adv. Mater. 2106540 (2022).

[7]M. T. Hörantner, T. Leijtens, M. E. Ziffer, G. E. Eperon, M. G. Christoforo, M. D. McGehee, and H. J. Snaith, ACS Energy Lett. **2**, 2506–2513 (2017).

[8]M. Boccard and C. Ballif, ACS Energy Lett. **5**, 1077–1082 (2020).

[9]H. Shen, D. Walter, Y. Wu, K. C. Fong, D. A. Jacobs, T. Duong, J. Peng, K. Weber, T. P. White, and K. R. Catchpole, Adv. Energy Mater. **10**, 1902840 (2020).

[10]T. Leijtens, K. A. Bush, R. Prasanna, and M. D. McGehee, Nat. Energy **3**, 828–838 (2018).

[11]J. Werner, B. Niesen, and C. Ballif, Adv. Mater. Interfaces **5**, 1700731 (2018).

[12]B. Chen, N. Ren, Y. Li, L. Yan, S. Mazumdar, Y. Zhao, and X. Zhang, Adv. Energy Mater. **12**, 2003628 (2022).

[13]Y.-H. Lin, N. Sakai, P. Da, J. Wu, H. C. Sansom, A. J. Ramadan, S. Mahesh, J. Liu, R. D. Oliver, and J. Lim, Science **369**, 96–102 (2020).

[14]S.-H. Turren-Cruz, A. Hagfeldt, and M. Saliba, Science **362**, 449–453 (2018).

[15]D. A. Neamen, *Semiconductor Physics and Devices: Basic Principles* (McGraw-Hill, 2003).

[16]L. Mazzarella, Y. H. Lin, S. Kirner, A. B. Morales-Vilches, L. Korte, S. Albrecht, E. Crossland, B. Stannowski, C. Case, and H. J. Snaith, Adv. Energy Mater. **9**, 1803241 (2019).

[17]S.-W. Lee, S. Bae, J.-K. Hwang, W. Lee, S. Lee, J. Y. Hyun, K. Cho, S. Kim, F. D. Heinz, and S. B. Choi, Commun. Chem. **3**(1), 37 (2020).

[18]Z. Song, S. C. Watthage, A. B. Phillips, G. K. Liyanage, R. R. Khanal, B. L. Tompkins, R. J. Ellingson, and M. J. Heben, Chem. Mater. **27**, 4612 (2015).

[19]M. C. Schubert, L. E. Mundt, D. Walter, A. Fell, and S. W. Glunz, Adv. Energy Mater. **10**, 1904001 (2020).

[20]A. Singh, P. K. Nayak, S. Banerjee, Z. Wang, J. T. W. Wang, H. J. Snaith, and K. Narayan, Sol. RRL **2**, 1700173 (2018).

[21]S. Valouch, M. Nintz, S. W. Kettlitz, N. S. Christ, and U. Lemmer, IEEE Photonics Technol. Lett. **24**, 596–598 (2012).

[22]N. Christ, S. W. Kettlitz, J. Mescher, and U. Lemmer, Appl. Phys. Lett. **104**, 053302–053321 (2014).

[23]M. Pazoki, A. Hagfeldt, and T. Edvinsson, *Characterization Techniques for Perovskite Solar Cell Materials* (Elsevier, 2019).

[24]J. Shi, D. Li, Y. Luo, H. Wu, and Q. Meng, Rev. Sci. Instrum. **87**, 123107 (2016).

[25]R. C. Rumpf, Prog. Electromagn. Res., Part B **35**, 241–261 (2011).

[26]L. A. Pettersson, L. S. Roman, and O. Inganäs, J. Appl. Phys. **86**, 487–496 (1999).

[27]P. Peumans, A. Yakimov, and S. R. Forrest, J. Appl. Phys. **93**, 3693–3723 (2003).

[28]M. Jošt, G. Matič, E. Köhnen, B. Li, B. Glažar, M. Jankovec, S. Albrecht, and M. Topič, Sol. RRL **5**, 2100311 (2021).

[29]D. Lan and M. A. Green, Appl. Phys. Lett. **106**, 263902 (2015).